

## Supplementary Information for

### Geometry underlies the mechanical stiffening and softening of an indented floating film

Monica M. Ripp, Vincent Démery, Teng Zhang, and Joseph D. Paulsen

E-mail: [jdpaulse@syr.edu](mailto:jdpaulse@syr.edu) or [tzhang48@syr.edu](mailto:tzhang48@syr.edu) or [vincent.demery@espci.psl.eu](mailto:vincent.demery@espci.psl.eu)

#### This PDF file includes:

- Supplementary text
- Figs. S1 to S5
- Table S1
- References for SI reference citations

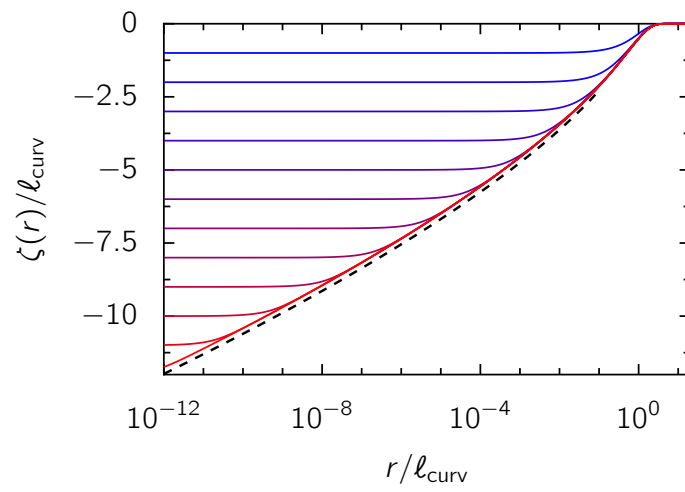


**Fig. S1.** Height profile from the numerical solution of the Euler-Lagrange equation for  $\delta \in \{1, 2, \dots, 12\}$  (blue to red solid lines) and asymptotic solution (Eq. (12), dashed black line).

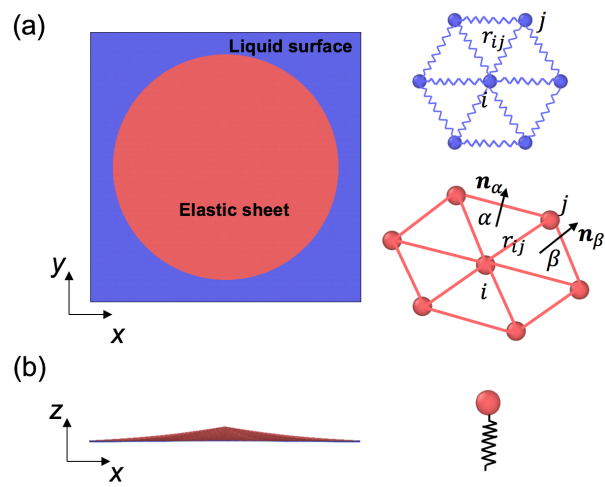


**Fig. S2.** Simulation model. **(a)** Top view of the simulation domain, and lattice elements for the liquid surface and the sheet. **(b)** Side view. Vertical displacements of the particles in the sheet are coupled to linear springs that impose a gravitational force.

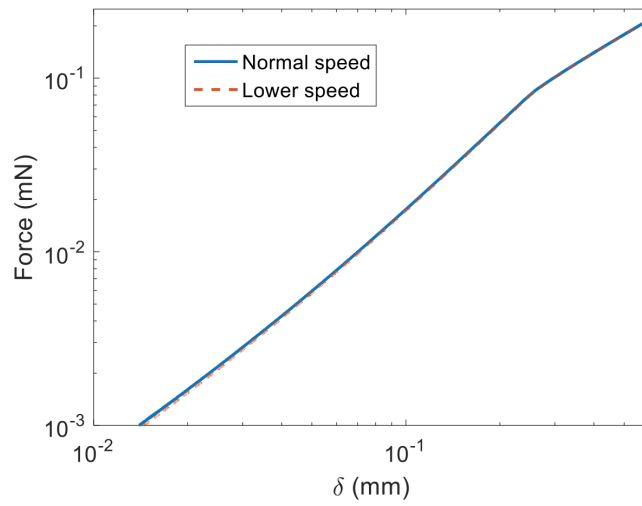


**Fig. S3.** Force versus indentation depth for two indenter speeds, measured in simulations with  $R = 6$  mm,  $t = 210$  nm,  $E = 0.73$  GPa,  $\gamma = 39$  mN/m,  $\rho = 909$  kg/m<sup>3</sup>. The curves are in good agreement, consistent with a quasistatic indentation process.

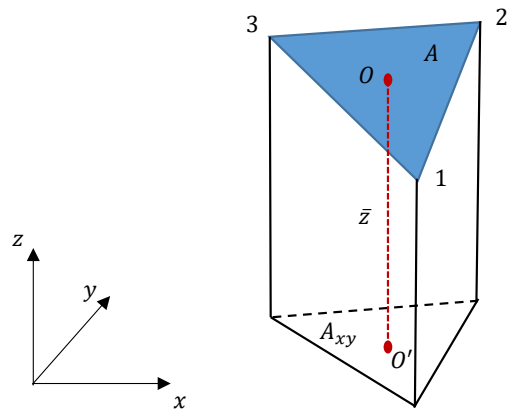


**Fig. S4.** Treatment of gravity in simulations reaching large slopes. The solid triangle represents a small element in the elastic thin sheet.  $O$  is the centroid of triangle, and  $O'$  is the centroid of the projected triangle on the  $x$ - $y$  plane.

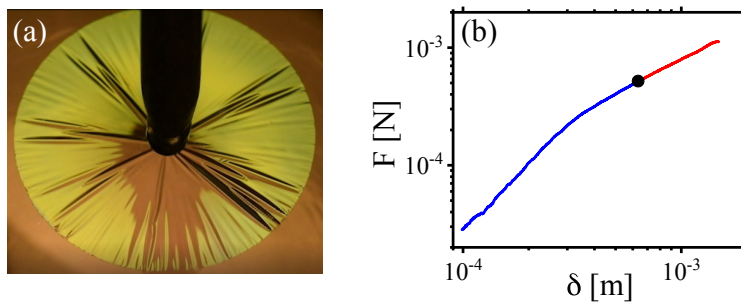


**Fig. S5.** Wrinkle-to-crumple transition. **(a)** Stress-focusing crumples appear at large indentation, as shown here at  $\delta = 1.08$  mm for a film with  $t = 437$  nm and  $R = 11$  mm. **(b)** The transition is not apparent in the force. (Black circle:  $\delta$  where crumples appear.) Here,  $t = 103$  nm and  $R = 11$  mm.

**Table S1. Simulation units in LAMMPS (native) and scaled results.**

	Bending stiffness	Length	Surface tension	Young's modulus	Gravity
LAMMPS units	eV	Å	$\text{eV}/\text{Å}^2$	$\text{eV}/\text{Å}^3$	$\text{eV}/\text{Å}^4$
Scaled units	$\alpha$ eV	$\beta$ Å	$(\alpha/\beta^2)$ $\text{eV}/\text{Å}^2$	$(\alpha/\beta^3)$ $\text{eV}/\text{Å}^3$	$(\alpha/\beta^4)$ $\text{eV}/\text{Å}^4$

## Supporting Information Text

### Geometric approach: Energy functional

The axisymmetric configuration is described by a function  $\zeta(r)$ , which describes the height of the sheet. The boundary condition at  $r = 0$  is given by the poking amplitude,

$$\zeta(0) = -\delta. \quad [1]$$

The sheet extends up to a radius  $W$ , which is given by length conservation:

$$\int_0^W \sqrt{1 + \zeta'(r)^2} dr = R. \quad [2]$$

In general, the boundary condition at  $W$  is given by continuity relations, and the profile of the liquid surface should be solved for. Here, we assume that the length over which the sheet is deformed is much smaller than  $R$  and we can write  $\zeta(W) = 0$ .

The energy is the sum of the gravitational energy,

$$U_{\text{gravity}} = \pi \rho g \int_0^W r \zeta(r)^2 dr, \quad [3]$$

and the surface energy, which is given by the excess area of the exposed liquid interface:

$$U_{\text{surface}} = \pi \gamma (R^2 - W^2); \quad [4]$$

we choose the convention so that  $U_{\text{surface}} = 0$  in the flat state.

Since we have assumed that  $\zeta(r) \simeq 0$  for  $r \sim W$ , we can extend the function  $\zeta(r)$  over  $[0, \infty]$ , and we can write

$$U_{\text{gravity}} = \pi \rho g \int_0^\infty r \zeta(r)^2 dr, \quad [5]$$

$$R - W = \int_0^\infty \left[ \sqrt{1 + \zeta'(r)^2} - 1 \right] dr. \quad [6]$$

If we assume that the inward motion of the edge of the film is much smaller than its radius, we get for the surface energy:

$$U_{\text{surface}} = \pi \gamma (R + W)(R - W) \simeq 2\pi \gamma R \int_0^\infty \left[ \sqrt{1 + \zeta'(r)^2} - 1 \right] dr. \quad [7]$$

Finally, the total energy is

$$U = U_{\text{gravity}} + U_{\text{surface}} = \pi \int_0^\infty \left( \rho g r \zeta(r)^2 + 2\gamma R \left[ \sqrt{1 + \zeta'(r)^2} - 1 \right] \right) dr, \quad [8]$$

and the boundary conditions are  $\zeta(0) = -\delta$ ,  $\lim_{r \rightarrow \infty} \zeta(r) = 0$ .

### Limiting shape at large indentation

Using  $\ell_{\text{curv}}$  as the unit length, the Euler-Lagrange equation for the profile reads

$$\zeta''(r) = r \zeta(r) [1 + \zeta'(r)^2]^{3/2}. \quad [9]$$

Here we determine the asymptotic behavior of the solution as  $r \rightarrow 0$  in the limit of infinite confinement,  $\lim_{r \rightarrow 0} \zeta(r) = -\infty$ . In this limit,  $|\zeta'(r)| \gg 1$  and the equation reduces to

$$\zeta''(r) = r \zeta(r) \zeta'(r)^3. \quad [10]$$

Writing the profile as  $\zeta(r) = f(\log(r))$ , the equation for  $f(u)$  is

$$f''(u) - f'(u) = f(u) f'(u)^3. \quad [11]$$

We have to determine which term dominates in the left hand side. If  $f''(u)$  dominates, we arrive at  $f'' = f f'^3$ , leading to  $f(u) \sim u^{1/3}$ ; but then  $f''(u) \ll f'(u)$  as  $u \rightarrow \infty$ , which is in contradiction with our assumption. We should thus assume that  $f'(u)$  dominates, leading to  $f(u) f'(u)^2 = -1$ , which is solved by  $f(u) = -(3u/2)^{2/3}$ , and

$$\zeta(r) \underset{r \rightarrow \infty}{\sim} - \left[ \frac{3}{2} \log \left( \frac{1}{r} \right) \right]^{2/3}. \quad [12]$$

This asymptotic shape is in very good agreement with the numerical integration of the Euler-Lagrange equation (Fig. S1).

## Simulation method

**Lattice model.** We developed a lattice based numerical model where the elastic sheet is described by a triangular lattice model (1), and the liquid surface tension is described by a spring with zero rest length (2). The total elastic energy of the triangular lattice model can be defined as a combination of the stretching energy and bending energy,

$$U_{\text{sheet}} = \frac{\sqrt{3}}{4}Y \sum_{ij} (r_{ij} - r_0)^2 + \frac{2}{\sqrt{3}}B \sum_{\alpha\beta} (1 - \mathbf{n}_\alpha \cdot \mathbf{n}_\beta) \quad [13]$$

where  $Y$  is the in-plane stiffness,  $B$  is the bending stiffness,  $r_{ij}$  is the current bond length,  $r_0$  is the equilibrium bond length, and  $\mathbf{n}_\alpha$  and  $\mathbf{n}_\beta$  are the normal vectors of nearest neighbors (Fig. S2a). The in-plane stiffness  $Y = Et$  and bending stiffness  $B = Et^3/(12(1 - \Lambda^2))$  of the thin sheet are defined in terms of the Young's modulus  $E$ , Poisson's ratio  $\Lambda$ , and film thickness  $t$ .

The liquid surface tension is modeled as zero-rest length spring, which tends to minimize the spring length and thus the total surface area. If the springs form an equilateral triangle, the spring constant can be directly linked to the surface tension as:

$$U_{\text{liquid}} = \frac{1}{2\sqrt{3}}\gamma \sum_{ij} r_{ij}^2. \quad [14]$$

We adopted a high resolution lattice model to make sure the deviations of the equilateral triangles are small. The gravity force was directly applied to the particles in the elastic sheet,

$$F_{\text{gravity}} = -\frac{\sqrt{3}}{2}r_0^2\rho g z, \quad [15]$$

where the force was only along  $z$  direction, and the coefficient represents the effective area of a particle in the triangular lattice model.

We embedded an elastic sheet in a liquid surface within a square simulation domain with periodic boundary conditions. All the simulations were carried out with molecular dynamics software LAMMPS. A small spherical indenter of radius 110  $\mu\text{m}$  was adopted in the simulation via the command "fix indent" in LAMMPS. The indenter was slowly moved at a constant speed to poke the elastic thin sheet, ensuring a quasi-static process. In the simulations, we first followed the metal units in LAMMPS and then scaled the quantities to physical spaces comparable to experiments. The key units directly used in the simulations are summarized in Table 1. We scale the energy unit by  $\alpha$  and the length unit by  $\beta$  to map the simulations onto a physical structure comparable to the experimental set up. The scaled units are shown in the second row of Table 1, with two adjustable parameters  $\alpha$  and  $\beta$ . In all the simulations, we set  $\alpha = 10^8$  and  $\beta = 1.2 \times 10^5$ . We use the scaled units in the main text.

During simulations, a Langevin thermostat was adopted to maintain a very low temperature (0.001 K in the simulation units). We also reduced the indenter speed for a typical simulation and did not observe significant change in the measured forces (Fig. S3), indicating that the speed of the indenter is sufficiently slow.

**Treatment of gravity at large slopes.** For the films with  $R = 44$  mm, we carried out our simulations to large amplitude where the sheet attains large slopes. This situation requires a modified treatment of the gravity force. A small triangular element in the elastic sheet will be tilted in the current deformed configuration (Fig. S4), effectively reducing the volume of liquid lifted by the solid film. The volume change due to the film deformation can be expressed as:

$$V = A_{xy}\bar{z}, \quad [16]$$

where  $A_{xy}$  is the projected area of the triangle on  $xy$  plane,  $\bar{z} = 1/3(z_1 + z_2 + z_3)$  is the height of the centroid (O) of the triangle. Therefore the gravity energy at large deformation can be written as:

$$U_{\text{gravity}} = \frac{1}{2}\rho g A_{xy}\bar{z}^2. \quad [17]$$

The force components applied on each node in the triangle can be calculated as:

$$f_x^i = -\frac{\partial U_{\text{gravity}}}{\partial x_i} = -\frac{1}{2}\rho g \bar{z}^2 \frac{\partial A_{xy}}{\partial x_i} \quad [18a]$$

$$f_y^i = -\frac{\partial U_{\text{gravity}}}{\partial y_i} = -\frac{1}{2}\rho g \bar{z}^2 \frac{\partial A_{xy}}{\partial y_i} \quad [18b]$$

$$f_z^i = -\frac{\partial U_{\text{gravity}}}{\partial z_i} = -\frac{1}{3}\rho g \bar{z} A_{xy} \quad [18c]$$

To avoid material penetration, a purely repulsive force is applied to particles in the solid film, such as:

$$f_{ij} = K_c \sin\left(\frac{\pi r}{r_c}\right); \quad (r < r_c), \quad [19]$$

where  $K_c$  controls the strength of the repulsive force,  $r_c$  is the cutoff of the interaction and the force is 0 for  $r > r_c$ .

## Experimental methods and analysis

**Film preparation.** We made polymer films by spin-coating solutions of polystyrene ( $M_n = 99\text{k}$ ,  $M_w = 105.5\text{k}$ , Polymer Source) in toluene (99.9%, Fisher Scientific) onto glass substrates, following Ref. (3). After the indentation, each film (or a portion of the film) was retrieved on a silicon wafer. Film thickness was then measured using a white-light interferometer (Filmetrics F3). Thicknesses were found to be uniform to within 2% when  $R = 11$  or  $22$  mm, and to within 3% when  $R = 44$  mm.

**Force measurements.** We measured normal forces using a custom setup that uses a capacitive sensor (PI PiSeca E-852 with D-510.020) to detect the deflections of a metal cantilever that pushes down on the sheet via a spherical indenter tip. This force probe is mounted on a computer-controlled vertical translation stage with a resolution of  $5\ \mu\text{m}$ . The apparatus was calibrated by hanging known masses from the indenter. We tested this calibration method with an independent measurement where we hung a Wilhelmy plate from the indenter tip and lowered it into water (ensuring full wetting of the water to the plate), and we recovered the surface tension of a clean air-water interface to within  $1\ \text{mN/m}$ .

To identify the moment of contact, we first examine the corresponding video to find its approximate time. The precise moment of contact is marked by a significant reduction in noise in the capacitive sensor signal. We set  $\delta = 0$  to coincide with this noise drop, and  $F = 0$  is found by averaging the force at earlier times.

**Measuring  $\delta^*$ .** Reference (4) defined  $\delta_*$  as the point where  $F/\delta^{3/2}$  is minimized. Here we measure  $\delta_*$  by collapsing the data to the empirical form  $F/F_* = \frac{1}{2}[\delta/\delta_* + (\delta/\delta_*)^2]$ , where  $F_*$  and  $\delta_*$  are free parameters for each measured curve. So long as there is sufficient data on each side of the crossover, the two methods are essentially equivalent, since the function  $(x + x^2)/x^{3/2}$  is minimized at  $x = 1$ . However, when determining  $\delta_*$  by our method, one must ensure that there is sufficient data on each side of the crossover in order to obtain reliable results.

## Crumpling transition

At large indentation depth beyond  $\delta_{**}$ , the previously-smooth wrinkled pattern becomes concentrated into a discrete set of deformations, as shown in Fig. S5a. This progression is similar to what is observed when a circular polymer sheet is placed on a droplet of gradually increasing curvature (5). These structures have been termed “crumples”, and their appearance marks a symmetry-breaking transition that is traversed as the indentation depth is varied, but their underlying physical mechanism is not understood (6). Crumples are observed at systematically smaller indentation for thicker films.

One might expect a signature in the normal force when crumples appear, since they are known to focus stress at their tips (7). Surprisingly, the data are featureless through this transition despite the two distinct morphologies, as shown in Fig. S5b. This observation can be partially justified in the far-from-threshold framework (8) by noting that both crumples and wrinkles allow compression with vanishing elastic cost.

## References

1. Seung H, Nelson DR (1988) Defects in flexible membranes with crystalline order. *Physical Review A* 38(2):1005.
2. Giomi L, Mahadevan L (2012) Minimal surfaces bounded by elastic lines in *Proc. R. Soc. A*. (The Royal Society), Vol. 468, pp. 1851–1864.
3. Huang J (2010) Wrinkling of floating thin polymer films. *Ph.D. Thesis*.
4. Vella D, Davidovitch B (2018) Regimes of wrinkling in an indented floating elastic sheet. *Phys. Rev. E* 98(1):013003.
5. Paulsen JD, et al. (2015) Optimal wrapping of liquid droplets with ultrathin sheets. *Nature materials* 14(12):1206–1209.
6. King H, Schroll RD, Davidovitch B, Menon N (2012) Elastic sheet on a liquid drop reveals wrinkling and crumpling as distinct symmetry-breaking instabilities. *Proceedings of the National Academy of Sciences* 109(25):9716–9720.
7. King H (2013) Ph.D. thesis.
8. Davidovitch B, Schroll RD, Vella D, Adda-Bedia M, Cerda EA (2011) Prototypical model for tensional wrinkling in thin sheets. *Proceedings of the National Academy of Sciences* 108(45):18227–18232.